PCCP

Accepted Manuscript

ROYAL SOCIETY OF CHEMISTRY

www.rsc.org/pccp

Resonant Raman Spectra of Molecules with Diradical Character: Multiconfigurational Wavefunction Investigation of Neutral Viologens

Julia Romanova, Vincent Liégeois, and Benoît Champagne*

Laboratoire de Chimie Théorique, Unité de Chimie Physique Théorique et Structurale (UCPTS), University of Namur, Rue de Bruxelles 61, 5000 Namur, Belgium

Abstract

The resonant Raman and UV/vis absorption spectra of two diradicaloïd compounds, methyl viologen and phenylene-extended viologen in their neutral state, have been simulated using multiconfigurational wavefunction methods. For methyl viologen, a good agreement with experiment is evidenced for the UV/vis absorption vibronic structure, provided dynamic correlation is accounted for to get the vibrational frequencies and normal modes. To some extent, the agreement with experiment is also good for the RR spectrum and the differences have been attributed to the presence in the experimental spectrum of surface-enhanced effects due to adsorption on the electrodes. As a result of inserting a phenylene group between the pyridinium units, the simulations have demonstrated that i) in the UV/vis absorption spectrum, the relative intensity of the second band with respect to the 0-0 band increases, ii) additional strong bands are observed in the RR spectrum, and iii) the RR excitation profiles of the phenylene-extended viologen present less structure than in the case of methyl viologen where the mode intensities can strongly depend on the incident light wavelength. These differences are signatures of the extension of the effective conjugation length as well as of the increase in diradical character.

Keywords: resonant Raman, vibronic coupling, CASSCF/CASPT2, diradical character, viologens

1. Introduction

Theoretical chemists aim at characterizing the structures and properties of molecules in their ground and excited electronic states. Owing to the number of application domains, i.e. photochemistry, photovoltaics, nonlinear optics, molecular electronics to cite a few, accurate theoretical description of electronic excited states has become a central field of investigation because it contributes to optimizing and tuning the molecular properties.[1] Excited state spectroscopies take also advantage of the simulation and interpretation of molecular signatures by quantum chemistry methods to unravel their structures and properties. Among these, UV/vis absorption and resonance Raman (RR) spectroscopies have benefited from many theoretical developments to evaluate the excitation energies, the transition dipole moments, the excited state energy gradients, and the vibrational normal modes and frequencies. Particularly challenging is the simulation of the RR spectra of π-conjugated systems that rely on an accurate description of the electron-phonon coupling. Still it provides detailed information on the structure and properties of electronic excited states as well as of the coupled ground state.[2]

During the last fifteen years, general approaches to simulate the RR spectra have been worked out and applied at different levels of approximation, encompassing the (time-dependent) Hartree-Fock [(TD)HF] and (time-dependent) density functional theory [(TD)DFT] approaches,[3] as well as high-level wavefunction methods[3g,4] like the second-order approximate coupled cluster singles and doubles (CC2) and restricted active space self-consistent field (RASSCF) methods. Although RR spectra of radical compounds have already been simulated by Lapouge *et al.*,[4a] to our knowledge, these methods have not yet been applied to diradical compounds. Owing to their remarkable properties in view of applications in electronics and nonlinear optics, diradical and multiradical compounds have attracted a renewed interest[5] and highlighting the diradical vibrational signatures remains a challenge.[6] This paper focuses on the simulation and interpretation of the RR and UV/vis absorption spectra of viologen derivatives (Scheme 1), whose neutral forms exhibit a degree of diradical character.

These bipyridinium derivatives are chosen because they possess a rich redox behavior.[7] The dication constitutes the most stable oxidation state, which can be converted into singly-reduced (radical cation) and doubly-reduced (neutral) forms. The redox transformations of viologens are

reversible and are accompanied by significant changes in their biological activity as well as in their optical, magnetic, and conducting properties. Therefore, viologens are regarded as multifunctional materials for application in molecular electronics, molecular switches and machines, solar cells, and herbicides.[8] A challenging aspect in viologens chemistry is the spectroscopic identification of the doubly-reduced neutral state. Since the electron-phonon coupling affects the π-conjugation of organic molecules, *in situ* RR spectroscopy appears as a method of choice.[2] In RR spectroscopy, incident light energy is in resonance with one (or several) electronic excited state(s), leading to a substantial increase in the Raman intensity of the vibrational modes describing the change of geometry upon electronic transition. In that context, quantum-chemical simulations turn out to be very useful to interpret the RR spectra and the associated UV/vis absorption spectra. Several quantum-chemical investigations on viologens have already tackled their geometrical structures, vertical excitation energies, infrared and off-resonant Raman spectra[9] but the resonance Raman and vibronic coupling effects in these compounds have so far been little studied. Recently, we assessed the performance of range-separated hybrid exchange-correlation (XC) functionals to simulate the RR and UV/vis absorption spectra of viologen derivatives in their cationic and radical cationic oxidation states.[10] However, these singly-excited determinants methods cannot be applied to neutral viologen species that exhibit diradical character and should be described by a multiconfigurational wavefunction. For instance, Navarrette *et al.*[9f] reported natural orbital occupation numbers (NOOC) for neutral biphenylene-extended viologen obtained with the complete active space self-consistent field (CASSCF) method and pointed out a significant singlet diradical proaromatic contribution to the electronic ground state.

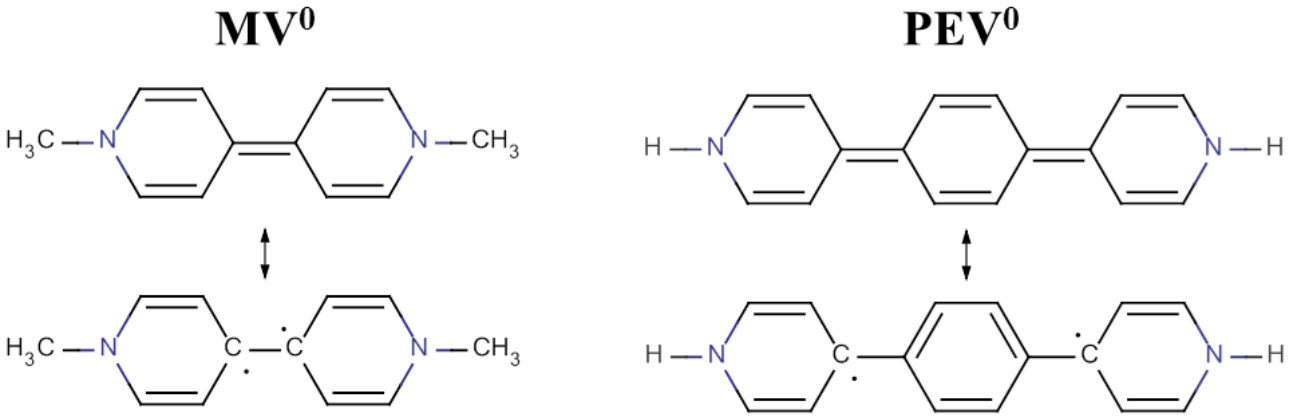

Scheme 1. Structures of neutral methyl viologen (MV^0) and phenylene-extended viologen (PEV^0).

In the present paper, the CASSCF and complete active space second-order perturbation theory (CASPT2) methods are employed to simulate and interpret the absorption and RR spectra of the neutral form of methyl viologen (MV^0) and phenylene-extended viologen (PEV^0) (Scheme 1). The theoretical results are discussed in the light of experimental data [Ref. 11-14]. To our knowledge, this is the first time that the resonance Raman signatures are simulated and interpreted for diradical species. The paper is organized as follows. Section 2 summarizes the main theoretical and computational aspects of the multiconfigurational and vibronic structure calculations. Section 3 presents and discusses the results before conclusions are drawn in Section 4.

2. Theoretical Frame and Computational Protocol

2.1 Electronic structure calculations

Prior to simulating the UV/vis absorption and RR spectra, quantum chemical calculations were performed to determine the optimized geometry, the vibrational normal modes and frequencies of the electronic ground state, the excitation energies and transition dipole moments, as well as the changes of geometry upon excitation. These were achieved at different levels of approximation. The multiconfigurational results were obtained with the MOLPRO 2012[15,16] quantum chemistry package, while the single reference MP2 results with Gaussian 09.[17] All the electronic structure calculations were performed with the 6-31+G* basis set. The geometry optimizations were carried out under C_{2v} symmetry constraint.

In the CAS calculations, the definition of the active space is an important step. MV^0 contains 14 π-electrons and 12 π-molecular orbitals (Figure S1). Nevertheless, calculations with state-specific (SS)- and state-averaged (SA)-CASSCF(14,12) method reveal small contributions to the static electron correlation energy from the two lowest-lying π-bonding orbitals (Figure S1). In the ground state, their natural orbital occupation numbers are larger than 1.98 and their removal from the active space affects negligibly the results (Table S1). Therefore, these orbitals were excluded from the active space and the calculations on MV^0 were carried out at the CAS (10,10) level. On the other hand, PEV^0 has 20 π-electrons and 18 π-molecular orbitals. Similarly to MV^0, the two lowest-

lying π-bonding orbitals (Figure S1) were excluded and the active space of PEV^0 was truncated to (16,16).

The ground state geometries of MV^0 and PEV^0 were optimized with the MP2 and SS-CASSCF methods, as well as with the two-state-averaged SA2-CASSCF method, where the ground state is mixed with the lowest-energy dominant excited state. In addition, the ground state of MV^0 was optimized with the SS-CASPT2 method. The $S_0 \rightarrow S_1$ vertical excitation energies of MV^0 and PEV^0 were calculated from single point SA2-CASPT2 calculations on the SA2-CASSCF ground state geometries. In order to avoid the intruder states problem, a level shift of 0.3 a.u. was applied. The electronic transition dipole moments μ_{0e} and the geometry of the first excited state were obtained at the SA2-CASSCF level. The normal modes and vibrational frequencies of the ground state of viologens were estimated at the MP2 and SS-CASSCF levels (only for MV^0). Real vibrational frequencies demonstrated that the geometry is a minimum on the potential energy surface.

2.2. Resonance Raman calculations

The resonance Raman and vibronic spectra were simulated within the transform theory (TT)[18] with a locally-developped program. These simulations are based on several assumptions: (1) the Born-Oppenheimer approximation is valid, (2) only the Condon scattering is important; (3) only one excited state is in resonance and it dictates the scattering mechanism, (4) ground and excited state potential energy surfaces are harmonic, (5) the normal coordinates of both states differ only in their equilibrium positions and the excited state potential surface is only displaced, i.e. the model neglects vibrational frequencies modifications in the excited state, as well as Duschinsky rotation effects, (6) the effect of the temperature is neglected and the initial state is the vibrational ground state, (7) resonance Raman intensities for overtone and combination bands are not taken into account. As a matter of fact, within TT, the resonance Raman intensity $I_{0\text{-}1_\ell}(\omega_\ell)$ for the fundamental transition $0 \rightarrow 1_\ell$ is proportional to the fourth power of the electronic transition moment (μ_{0e}) and to a frequency dependent term $\Phi(\omega_L)$:

$$I_{0\text{-}1_\ell}(\omega_\ell) \propto \mu_{0e}^4 \omega_L (\omega_L - \omega_\ell)^3 \frac{\Delta_\ell^2}{2} \left| \Phi(\omega_L) - \Phi(\omega_L - \omega_\ell) \right|^2 \quad (1)$$

where ω_L is the frequency of the incident light, ω_ℓ is the frequency of the ℓ^{th} normal mode, $\Delta_\ell^2/2$ is the Huang-Rhys factor of mode ℓ, and Δ_ℓ represents a dimensionless displacement along the ℓ^{th} normal coordinate when going from the ground to the excited state potential minimum. The frequency dependent term reads:

$$\Phi(\omega_L) = \sum_{\nu} \frac{\prod_i^{3N-6} \left|\left\langle \theta_{g0_i} \middle| \theta_{ev_i} \right\rangle\right|^2}{\omega_{g0,e0} + \sum_j^{3N-6} \nu_j \omega_j - \omega_L - i\Gamma}, \qquad (2)$$

where $\omega_{g0,e0}$ is the frequency of the origin transition, Γ is a damping factor describing the homogeneous broadening, $\left|\left\langle \theta_{g0_i} \middle| \theta_{ev_i} \right\rangle\right|^2$ are the Franck-Condon (FC) factors and the summation runs over all vibrational quantum numbers ν_i of the electronic excited state. $\left\langle \theta_{g0_i} \middle| \theta_{ev_i} \right\rangle$ represents a one-dimensional overlap integral between the vibrational wavefunctions of mode i in the electronic and vibrational ground state $\left|\theta_{g0_i}\right\rangle$ and in a vibrational state of the electronic excited state $\left|\theta_{ev_i}\right\rangle$. The dimensionless displacements (Δ_ℓ) are calculated within the independent mode displaced harmonic oscillator model (IMDHOM), which is based on the assumptions (4) and (5), i.e. they are evaluated from the ground state vibrational frequencies (ω_ℓ) and normal modes, as well as from the differences between the ground and excited state geometries. Once the Δ_ℓ are obtained, the FC overlap integrals are computed by using recursive relations.[19] Then, the frequency dependent term $\Phi(\omega_L)$ is calculated and the RR spectra are simulated. The imaginary part of $\Phi(\omega_L)$ is also used for obtaining the vibronic structure of the UV/vis absorption spectra $A(\omega_L)$ through:

$$A(\omega_L) \propto \omega_L \, \mu_{0e}^2 \, Im\left[\Phi(\omega_L)\right]. \qquad (3)$$

Several thousands of FC factors are considered to get converged RR and absorption spectra (sum of FC factors ≥ 0.980). The Γ damping factor in Eq. 2 was set to 0.05 eV for the RR spectra and to 0.07/0.05 eV for the UV/vis spectra of MV^0/ PEV^0.

3. Results and Discussion

3.1. Methyl viologen

Representative geometrical parameters of the optimized structures of the ground and excited states of MV^0, obtained with different methods, are given in Table 1. With all methods, the ground

state of MV^0 presents a typical quinoid structure where both the C^1-C^2 intra-ring and C^3-$C^{3'}$ inter-ring bonds display a double bond character while the pyridine rings are coplanar. The nitrogen atoms are slightly pyramidized, having $\theta_{Me/Py}$ dihedral angles of 150-160° that describe the deviation of the methyl substituents from the plane of the molecular skeleton. This demonstrates that the N lone pair does not fully participate to π-conjugation. Indeed, among the three MV oxidation states, in its electronic ground state, MV^0 has the most pronounced quinoid character compared to MV^{2+} and $MV^{\bullet+}$ (Table S1), which are described as fully aromatic and moderately quinoid, respectively. The bond length alternation (BLA) in MV^0, defined as ½[{d(C^2-C^3)-d(C^3-$C^{3'}$)} + {d(C^2-C^3)-d(C^1-C^2)}] depends on the method. So, CASSCF, which includes only static correlation, gives larger localization and BLA (BLA = 0.10-0.11 Å) than MP2 and CASPT2 (BLA = 0.08 Å), which also take into account dynamical correlation. As a matter of fact, the SS- and SA2-CASSCF (MP2 and SS-CASPT2) methods give very similar ground state geometries. Dynamic electron correlation effects are therefore important for an accurate prediction of MV^0 ground state geometry. The major electronic configurations of the MV^0 ground state are |22222 00000> and |22220 20000> with coefficients of 0.90 and -0.16, respectively (Figure S1). The latter indicates that the MV^0 ground state possesses a non-negligible diradical character. Note that going from a (10,10) to (14,12) active space does not change the SS-CASSCF optimized bond lengths by more than 0.004 Å (Table S1).

MV^0 undergoes a quinoid-to-aromatic transformation upon excitation to its first excited state, as predicted by SA2-CASSCF. Indeed, the double-like character of the inter-ring CC bond strongly decreases upon excitation, together with the BLA (BLA = 0.04 Å) and the nitrogen pyramidalization ($\theta_{Me/Py}$ = 171°). These geometrical changes are therefore expected to be visible on the RR spectra. The excited state of MV^0 has an important diradical character and it is dominated by two equally-contributing electronic configurations, |2222a b0000> and |2222b a0000>, with coefficients of 0.65. Thereof, the quinoid-to-aromatic transformation matches also the HOMO and LUMO topologies (Figure S1).

The SA2-CASPT2 vertical excitation energies of MV^0 are in good agreement with the experimentally observed absorption maximum (Table 2). The transition dipole moments are also listed but no experimental value is available. The simulated absorption spectra are presented in

Figure 1. They were obtained by using SA2-CASSCF ground and excited state geometries in combination with MP2 or SS-CASSCF ground state vibrational normal modes. For simplification, hereafter the projection on the MP2 normal modes is referred to as the *MP2 approach*, while the projection on the SS-CASSCF normal modes is denoted as the *CASSCF approach*. Table 3 summarizes the calculated and experimental ground state vibrational frequencies as well as the calculated HR factors. Since intruder states problems prevented to optimize the S_1 geometry at the CASPT2 level, the Δ_ℓ values were evaluated in a balanced way from both S_0 and S_1 state SA2-CASSCF optimized geometries rather than by combining S_0 geometry obtained at the SS-CASPT2 or MP2 level with S_1 SA2-CASSCF geometry.

Table 1. Optimized bond lengths R [Å] and dihedral angles θ [°] for the ground (S_0) and excited (S_1) states of MV^0, obtained at the single reference MP2 level and using multiconfigurational methods with a (10,10) active space.

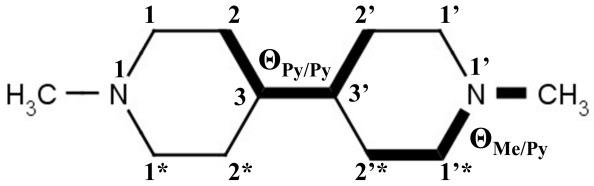

	S_0				S_1
	MP2	SS-CASSCF	SS-CASPT2	SA2-CASSCF	SA2-CASSCF
R(Me-N)	1.456	1.446	1.457	1.447	1.441
$R(N^1\text{-}C^1)$	1.393	1.395	1.395	1.397	1.373
$R(C^1\text{-}C^2)$	1.362	1.349	1.361	1.352	1.373
$R(C^2\text{-}C^3)$	1.453	1.469	1.454	1.466	1.437
$R(C^3\text{-}C^{3'})$	1.391	1.372	1.393	1.378	1.424
θ(Me/Py)	157	153	158	151	171
θ(Py/Py)	0	0	0	0	0

Table 2. Vertical excitation energy E_{0e} [eV], wavelength λ_{0e} [nm], and transition dipole moment μ_{0e} [a.u.] of MV^0 as determined using multiconfigurational approaches and (10,10) active space. The characteristics of the experimental absorption maximum measured in CH_2Cl_2 solution are listed for comparison.

	SA2-CASSCF	SA2-CASPT2	Exp. [11]
E_{0e}	5.65	3.28 †	3.11
λ_{0e}	219	378	398
μ_{0e}	3.13 †		

† Used for the simulations of RR and absorption spectra.

A very good agreement between the experimental[11] and theoretical absorption spectra of MV^0 is obtained when the Δ_ℓ are calculated using the MP2 normal modes (Figure 1 and Figure S2). The absorption band is characterized by two intense vibronic peaks, at 376 (maximum) and 358 nm, and by a shoulder at 333 nm. The most intense peak is mainly associated with the 0-0 transition but also with fundamental vibrational excitations of modes 10, 11, and 29 as well as with the overtone $2\nu_{10}$. The peak at 358 nm represents the second most significant peak in the spectrum and its intensity is very close to the absorption maximum. It mostly originates from the fundamental excitations of modes 63, 60, and 35 and from the combined excitation of modes 10 and 63. The shoulder at 333 nm is associated mainly with the overtone $2\nu_{63}$ and several combinations of bands: $\nu_{60}+\nu_{63}$, $\nu_{10}+2\nu_{63}$, and $\nu_{10}+\nu_{60}+\nu_{63}$. More details about the FC amplitudes are given in SI. On the other hand, the *CASSCF approach* fails to reproduce the experimentally-observed band shape because it predicts a single vibronic band peaking at 358 nm. This band originates from the 0-0 transition, from the fundamental excitation of modes 10, 29, 46, and 63 as well as from the overtone $2\nu_{29}$. The corresponding modes are sketched in Figure 2.

Figure 1. Simulated absorption spectrum of MV^0 and molecular orbitals involved in the electronic transition. The results were obtained by using SA2-CASSCF ground and excited state geometries in combination with MP2 (left) and SS-CASSCF (right) ground state vibrational normal modes.

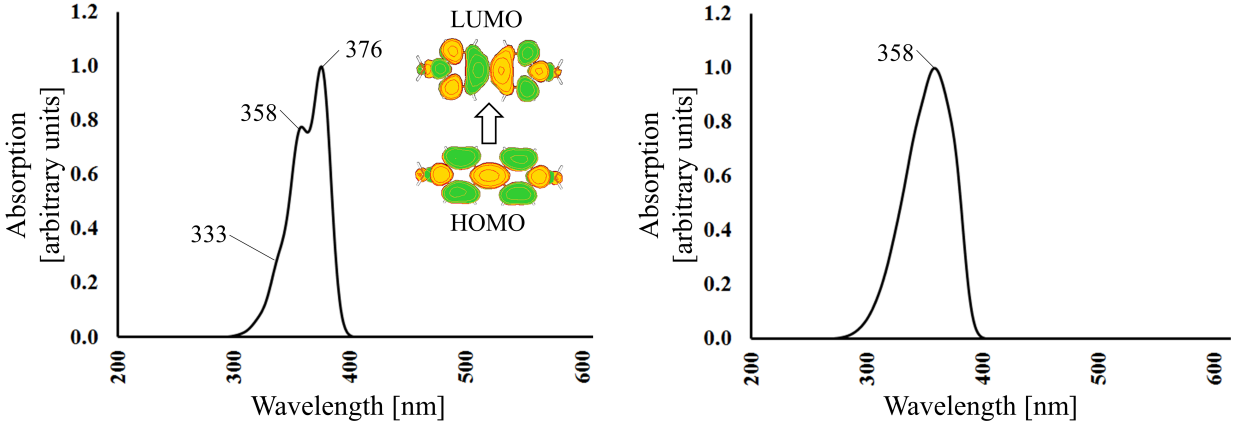

Figure 2. Sketches of the atomic displacements of the vibrational normal modes of MV^0 and PEV^0 having significant contributions to the vibronic and RR spectra. The direction of the atomic displacements is perpendicular to the junction planes between the two hemispheres of distinct color, and their amplitudes are proportional to the radius of the sphere. The sum of the surfaces of the spheres is always constant. The mode labels correspond to the increasing order of MV^0 frequencies while for PEV^0 they are determined by the similarity with the MV^0 modes.

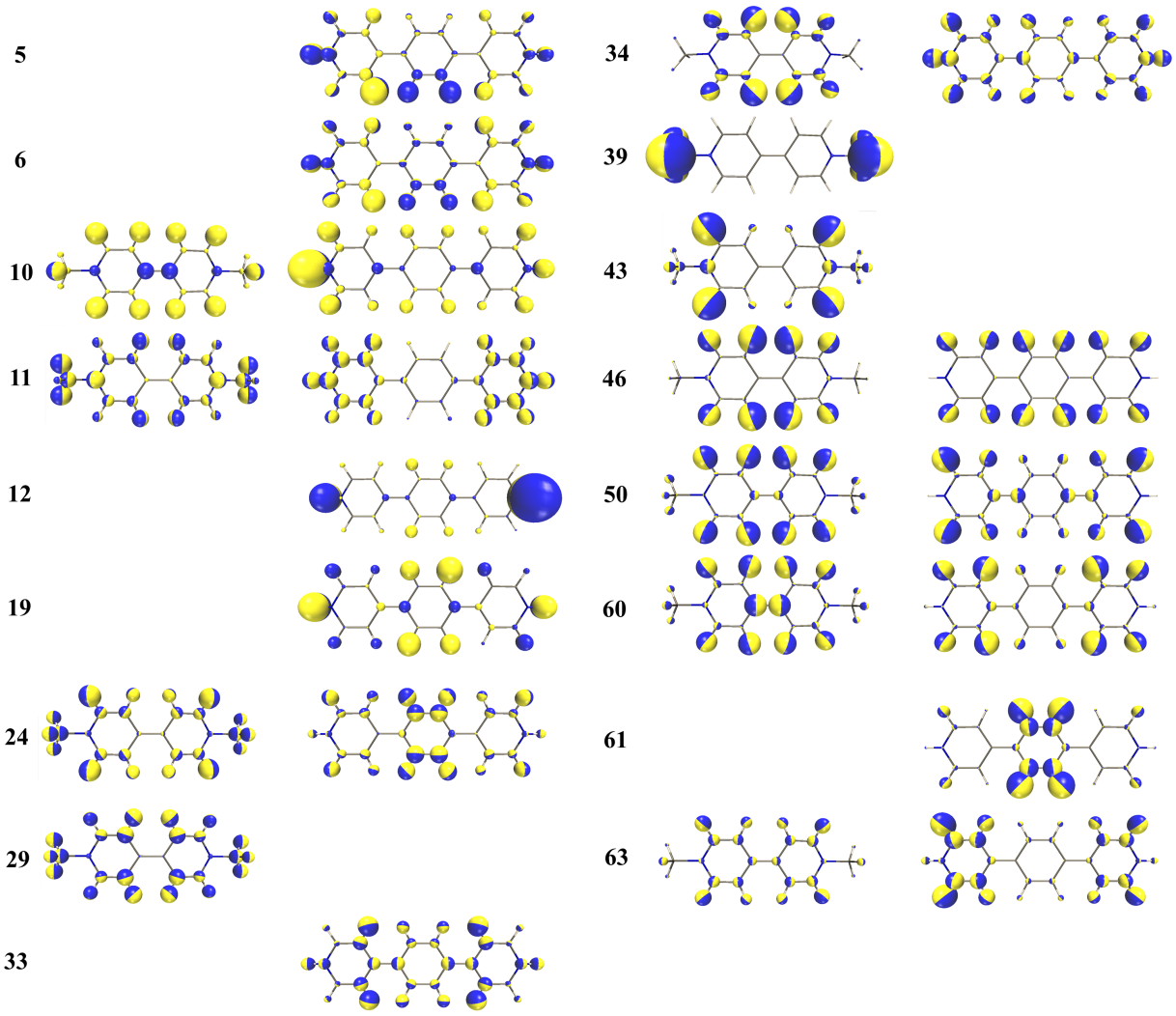

The resonance Raman spectra of MV^0 simulated using the *MP2 approach* are given in Figure 3 for different resonance conditions. Spectra simulated using the *CASSCF approach* and experiment are given in Figure S3. After accounting for a 0.970 scaling factor to correct the vibrational frequencies for anharmonicity effects, the *MP2 approach* predicts very accurately the position of the Raman bands with a root-mean-square deviation (RMSD) of ~4 cm^{-1} (the experimental band at 1607 was not considered). This agreement is consistent with the high similarities between the MP2 and CASPT2 geometries. On the other hand, owing to missing dynamic electron correlation, the scaling factor for the CASSCF frequencies is as small as 0.912.

After this correction, the RMSD amounts to ~14 cm^{-1}. Note that none of the two theoretical approaches predicts the RR band at 1607 cm^{-1}. The following discussion considers first the RR spectra obtained using the *MP2 approach* and then, a brief comparison is done with those simulated using the CASSCF normal modes.

Table 3. Mode labels, vibrational frequencies ω_ℓ [cm^{-1}], and Huang-Rhys factors S_ℓ for the 1st excited state of MV^0 and PEV^0 calculated with the MP2 and SS-CASSCF methods. Only the normal modes with significant Huang-Rhys factors are displayed (see Table S3 for more modes). Experimental vibrational frequencies of MV^0 are listed for comparison. The mode labels correspond to the increasing order of MV^0 frequencies while for PEV^0 they are determined by the similarity with the MV^0 modes.

	MV^0				MV^0		PEV^0	
	MP2		SS-CASSCF		Experiment		MP2	
Label	$\omega_{sc.*}$	S_ℓ	$\omega_{sc.**}$	S_ℓ	RR[12,13]	SERR[14]	$\omega_{sc.*}$	S_ℓ
5							70	0.188
6							109	0.317
10	241	0.393	291	0.229			268	0.449
11	277	0.093	270	0.035			218	0.132
12							335	0.738
19							431	0.136
21							492	0.098
24	668	0.012	652	0.172	676		743	0.074
29	791	0.177	766	0.803				
32	812	0.008	852	0.020				
33							947	0.063
34	994	0.085	976	0.124	996		987	0.120
						1199		
39	1133	0.063	1139	0.042				
43	1215	0.079	1200	0.080	1214			
						1237		
46	1254	0.028	1245	0.202	1245		1234	0.154
50	1389	0.010			1387		1363	0.066
54			1467	0.027				
						1522		
60	1545	0.097	1548	0.150	1543		1472	0.108
61							1565	0.107
						1606		
63	1660	0.349	1659	0.287	1659		1658	0.168

* after applying a scaling factor of 0.970
** after applying a scaling factor of 0.912

Figure 3. Resonance Raman spectra of MV^0 as obtained for different incident light energies as simulated by using SA2-CASSCF ground and excited state geometries in combination with MP2 ground state vibrational normal modes. The energies are successively set to E_{0e}-0.17 eV (399 nm), E_{0e}-0.09 eV (389 nm), E_{0e} (378 nm), E_{0e}+0.09 eV (368 nm), E_{0e}+0.17 eV (358 nm), E_{0e}+0.30 eV (345 nm, corresponding to the experimental conditions of Ref. 12), E_{0e}+0.39 eV (337 nm) and E_{0e}+0.47 eV (330 nm). The Raman bands are represented by Lorentzian functions with FWHM set to 10 cm^{-1}.

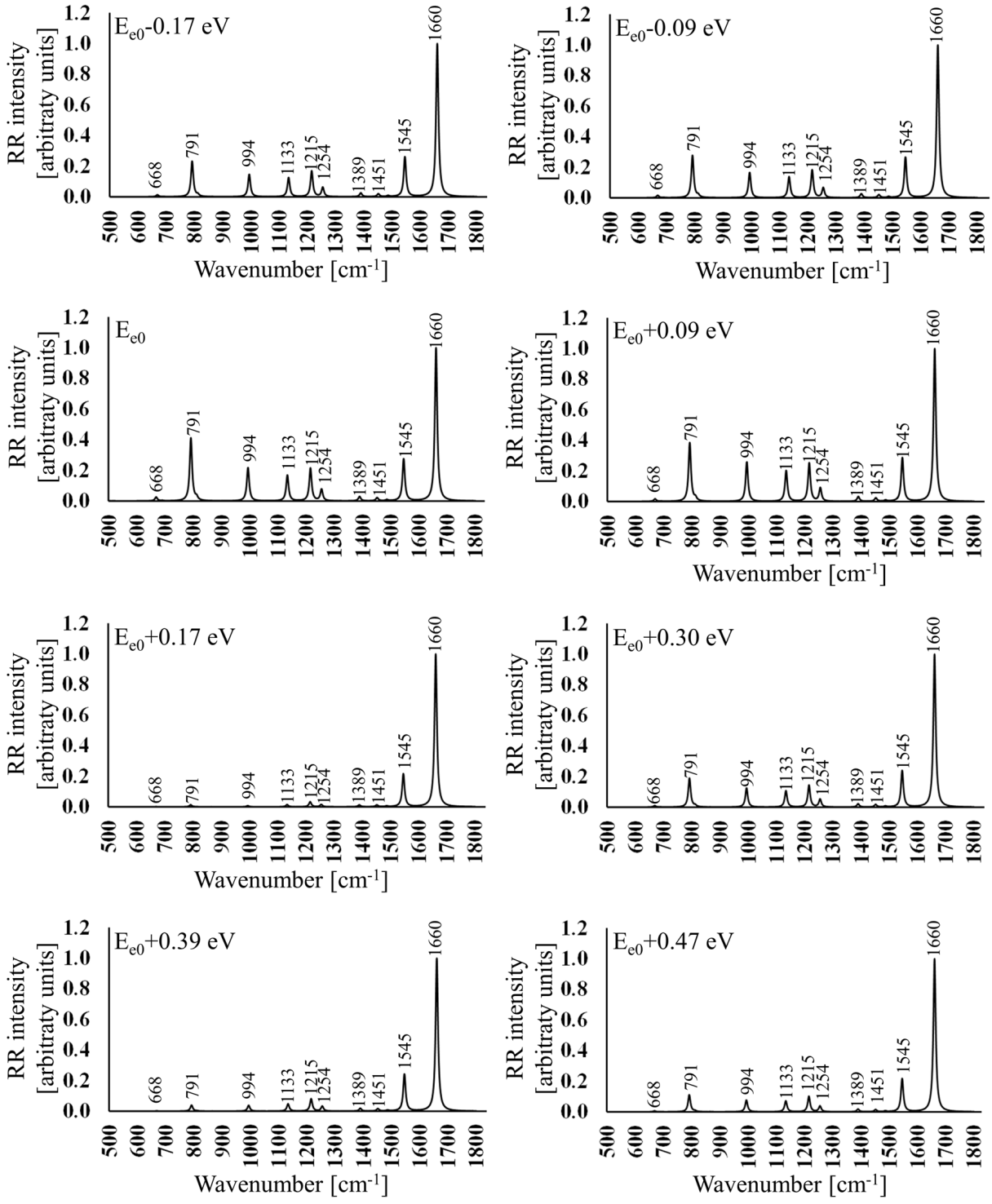

Figure 4. Resonance Raman excitation profiles for representative modes of MV^0 as simulated by using the SA2-CASSCF ground and excited state geometries in combination with MP2 ground state vibrational normal modes. Lines are used as guides to the eyes.

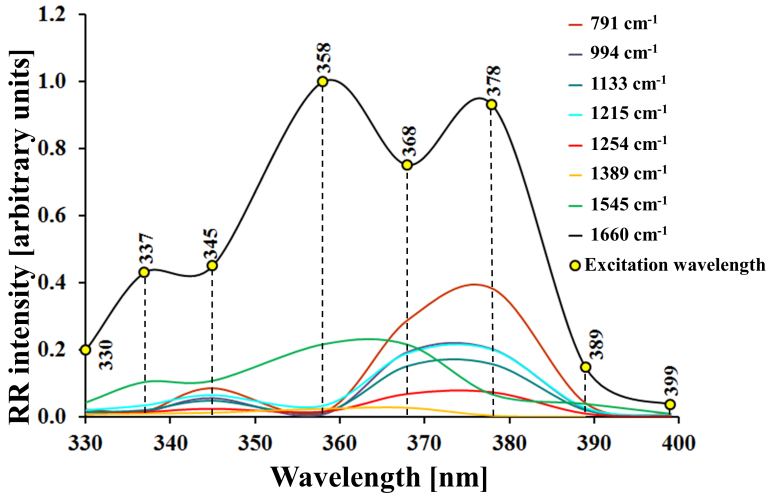

At E_{0e} (378 nm) the RR signatures of MV^0 consist of two bands above 1250 cm^{-1} [1545 cm^{-1} (modes 60) and 1660 cm^{-1} (mode 63)] while the region below 1250 cm^{-1} is characterized by several peaks, located at 1215 cm^{-1} (mode 43), 1133 cm^{-1} (mode 39), 994 cm^{-1} (mode 34), as well as at 791 cm^{-1} (mode 29). The latter one is also the second most intense peak in the RR spectrum at E_{0e}. When exciting at a slightly larger [at E_{0e}-0.17 eV (399 nm) and E_{0e}-0.09 eV (389 nm)] or smaller [E_{0e}+0.09 eV (368 nm)] wavelength, which corresponds to excitation in the same main absorption band, the RR signatures change little. The main impact is a decrease of the relative intensity of mode 29. On the other hand, when the excitation wavelength coincides with the second absorption band maximum [E_{0e}+0.17 eV (358 nm)], the RR spectrum reduces to the bands of modes 60 and 63. Then, going to smaller wavelength [E_{0e}+0.30 eV (345 nm)], several bands recover relative intensity whereas they get less intense again when the excitation wavelength matches the shoulder of the absorption spectrum [E_{0e}+0.39 eV (337 nm) and E_{0e}+0.47 eV (330 nm)]. These variations of the relative RR intensities of the dominant modes can be understood by analyzing the RR excitation profiles (Figure 4). Indeed, modes 60 (~1545 cm^{-1}) and 63 (~1660 cm^{-1}) have similar excitation profiles with larger (smaller) intensities at 337, 358 and 377 (330, 345, and 368) nm, which differ from those of the other modes.

The simulations can be compared with experiment, but only for the excitation energy of E_{0e}+0.30 eV (345 nm) (Figure S3). This comparison is, however, not straightforward. According to

the MP2 results the most intense RR band is located at ~1660 cm^{-1} (mode 63), which is in perfect agreement with the experimental spectrum observed in solution (band at 1659 cm^{-1}). This mode involves intra- and inter-ring CC stretching as well as CCH wagging motions and it has been theoretically and experimentally demonstrated to be also the most intensive band in the (non)-resonant Raman spectra of MV^{2+} (476.2 nm) and $MV^{\bullet+}$ (350.6 nm), respectively.[20] The second peak in decreasing order of intensity is located at 1543 cm^{-1} and the next one at 996 cm^{-1}. They are predicted by the simulation [at 1545 cm^{-1} (mode 60) and at 994 cm^{-1} (modes 34)] but their relative RR intensities are underestimated. On the other hand, the simulations also predict RR bands at 1389 cm^{-1} (mode 50), 1254 cm^{-1} (mode 46), 1215 cm^{-1} (mode 43), 791 cm^{-1}(mode 29), and 668 cm^{-1} (modes 24) whereas these are mostly hidden by the fluorescence background in the experimental spectrum, which makes difficult the assessment of the performance of the theoretical approaches.

As shown in Figure S3, the *CASSCF approach* gives similar results for modes 63, 60, and 34 while it overestimates the relative RR intensities for the bands at 766 cm^{-1} (mode 29) and 1245 cm^{-1} (mode 46). To a given extent, the CASSCF spectrum disagrees with respect to experiment more than the MP2 spectrum because if the 1245 cm^{-1} band can be hidden by fluorescence, the predicted HR factor for the band at 766 cm^{-1} is so large that it should be observed.

Two explanations can be raised to explain the differences between the experimental and RR spectra simulated with the *MP2 approach, i.e.* (i) MV^0 can adsorb on the electrode or (ii) it MV^0 can adopt a high-spin (triplet) state, both giving rise to modified or new RR signatures. The first hypothesis relies on the electron-rich and strong reducer character of MV^0, which is detected at low electrode potential in spectroelectrochemical measurements. Indeed, it has been demonstrated that MV^0 can both physisorbed and chemisorbed on the electrode.[14] As a result, in addition to the RR effects, surface-enhanced (SE) effects appear. These SERR effects are so strong that they enable the detection of MV^0 even at very low concentrations, immediately after the electrode potential is switched on. When a molecule is chemisorbed, a charge transfer occurs between the MV^0 and the electrode, which not only affects the relative intensities of the RR bands but also leads to band shifts. This hypothesis, which can explain the experimentally observed band at 1609 cm^{-1}, is supported by the following facts: (i) the MV^0 vibrational normal mode analysis due to Ghoshal *et al.*[13] predicts only two Raman bands above 1500 cm^{-1} (1674 cm^{-1} and 1553 cm^{-1}), which is consistent with the MP2 (1660 cm^{-1} and 1545 cm^{-1}) and CASSCF (1659 cm^{-1} and 1548 cm^{-1})

calculations; (ii) the dication and the radical cation forms of methyl viologen also possess only two Raman bands above 1500 cm^{-1}, MV^{2+} (1538 cm^{-1} and 1654 cm^{-1}) and $MV^{\bullet+}$ (1534 cm^{-1} and 1662 cm^{-1})[10]; (iii) on the other hand, the solution RR spectrum (363.8 nm) of MV^0 prepared by electrolysis is characterized by three Raman bands above 1500 cm^{-1} (1659 cm^{-1}, 1607 cm^{-1} and 1543 cm^{-1})[12]; and (iv) the same three bands are also visible in the SERR spectrum[14] (363.8 nm) of MV^0 recorded on silver electrode but in this case the 1607 cm^{-1} band has a similar intensity to the bands at 1659 cm^{-1} and 1543 cm^{-1}; (v) moreover, the I_{1545}/I_{1660} ratio in the simulated spectra of MV^0 varies between 0.22 and 0.29 as a function of the excitation wavelength (Figure 3), while it amounts to about 1.00 in the experimental spectrum (Figure S3), demonstrating that the large experimentally observed I_{1545}/I_{1660} ratio is related to surface enhancement effects. In addition, a band at 1579 cm^{-1} was experimentally observed in the SERR spectrum of neutral heptylviologen (HV^0) adsorbed on silver electrode[21] and the authors explained its presence as resulting from a shift of the main Raman peak at ~1651 cm^{-1} (corresponding to the 1659 cm^{-1} in MV^0) due to a charge transfer to metal.

The second hypothesis follows the recent work by Lopez-Navarette *et al.*[9f], who have reported experimental and CASSCF Raman spectra for the singlet and the triplet states of biphenylene-extended viologen (BEV^0). Their theoretical results demonstrate that in its singlet state BEV^0 is characterized by only two Raman bands above 1490 cm^{-1}, at 1498 cm^{-1} (exp. 1500 cm^{-1}) and at 1635 cm^{-1} (exp. 1642 cm^{-1}), like in the present calculations on MV^0. However, the experimental spectrum of BEV^0 displays three more bands, at 1593 cm^{-1}, 1587 cm^{-1}, and 1535 cm^{-1}. Owing to the prediction, at the CASSCF level, of frequencies at 1590 cm^{-1}, 1584 cm^{-1}, and 1521 cm^{-1}, these three bands were attributed to the triplet form. Then, by superimposing the simulated Raman spectra of the singlet and triplet forms of BEV^0, a very good agreement between simulation and experiment was achieved. Their hypothesis was substantiated by the small singlet-triplet energy difference ($\Delta E_{S0\text{-}T1}$ ~ 3 kcal/mol at CASPT2 level), which allows thermally-activated population of the first triplet state at room temperature as well as by experimentally observed temperature dependence of the Raman spectra. However, for MV^0, the SS-CASPT2 calculations predict $\Delta E_{S0\text{-}T1}$ ~ 42 kcal/mol (or ~34 kcal/mol at using SA2-CASPT2 optimization), which excludes the thermally-activated S_0 to T_1 intersystem crossing, as an explanation for the differences between the simulated and experimental RR spectra.

3.2. Phenylene-extended viologen

PEV^0 is structurally similar to MV^0. However, the phenylene extension between the heterocycles allows to gain insight into the effect of conjugation length on the vibronic coupling in diradicals. Table 4 summarizes the optimized geometrical parameters for its ground and excited states obtained with the MP2 and SA2-CASSCF methods. Similarly to MV^0, the ground state structure of PEV^0 is quinoid, while the excited state presents some aromatic character. Still, the ground state of PEV^0 displays larger aromatic character than MV^0, which is consistent with the elongation of the conjugation path (Table 4). The latter is confirmed by a decrease of the BLA going from MV^0 (S_0) to PEV^0 (S_0), which amounts to 0.03 Å and 0.01 Å at the MP2 and SA2-CASSCF levels (The BLA of PEV^0 is defined as 1/4[{d(C2-C3)-d(C1-C2)} + {d(C2-C3)-d(C3-C4)} + {d(C4-C5')-d(C3-C4)} + {d(C4-C5')-d(C5-C5')}]. On the other hand, the SA2-CASSCF method predicts the same BLA values for the excited states of both viologens.

Table 4. Optimized bond lengths R [Å] and dihedral angles θ [°] for the ground (S_0) and first excited (S_1) states of PEV^0, obtained at the single reference MP2 level and using multiconfigurational methods with a (16,16) active space.

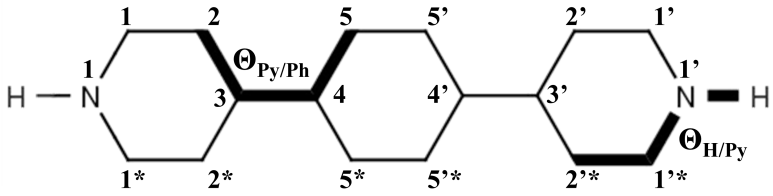

	S_0			S_1
	MP2	SS-CASSCF	SA2-CASSCF	SA2-CASSCF
$R(N^1\text{-}C^1)$	1.385	1.391	1.393	1.372
$R(C^1\text{-}C^2)$	1.364	1.350	1.350	1.369
$R(C^2\text{-}C^3)$	1.448	1.467	1.466	1.439
$R(C^3\text{-}C^4)$	1.410	1.386	1.389	1.430
$R(C^4\text{-}C^5)$	1.437	1.456	1.453	1.434
$R(C^5\text{-}C^{5'})$	1.375	1.360	1.362	1.377
θ(H/Py)	169	156	155	180
θ(Py/Ph)	3	1	1	0

The simulated absorption and resonance Raman spectra of PEV^0 obtained by the *MP2 approach* are presented in Figures 5, 6, and 7 whereas details on the first vertical excitation are given in Table S2. The first excited state is mostly characterized by a HOMO-LUMO transition, whose topologies (Figure 5) substantiate its quinoid-to-aromatic character. The *MP2 approach* predicts similar absorption band shapes for both PEV^0 and MV^0. Nevertheless, with respect to MV^0 the absorption maximum is bathochromically shifted by 1.03 eV whereas the relative intensity of the so-called "0-1" band with respect to the "0-0" band is larger (I_{492}/I_{518} = 0.95 with respect to I_{358}/I_{376} = 0.80 for MV^0). This result is explained from the increase of the conjugation length (Tables 1 and 4) and the increase of the aromatic character upon the insertion of a phenylene bridge. The main vibronic peak of PEV^0 is located at ~518 nm, close to the 0-0 transition and it originates from the 0-0 transition, from the fundamental excitations of modes 6, 10 and 12, as well as from their simultaneous excitations, $\nu_{10}+\nu_{12}$ and $\nu_6+\nu_{12}$. Smaller but still important contributions to this peak come from modes 5, 11, and 19. The second vibronic peak at ~492 nm results from fundamental excitation of modes 34, 46, 60, 61, and 63 and in this region ν_{63} dominates. In addition, many combinations of bands, involving the above mentioned modes also contribute to the second peak. Then, the shoulder at ~450 nm originates entirely from combination bands and overtones.

Figure 5. Simulated absorption spectrum of PEV^0 and molecular orbitals involved in the electronic transition. The results were obtained by using SA2-CASSCF ground and excited state geometries in combination with MP2 ground state vibrational normal modes.

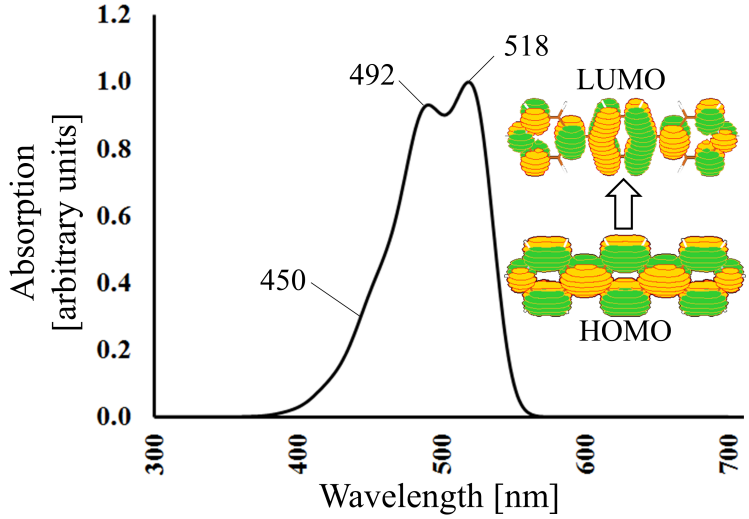

The RR spectra of PEV^0 obtained at different resonance conditions by the *MP2 approach* are presented in Figure 6. The comparison between the RR spectra of PEV^0 and MV^0 reveals that at same resonance conditions a larger number of strong bands is observed in the extended viologen and that the spectra are less sensitive to the energy of the incident light. The latter fact originates from the similar excitation profiles (Figure 7) observed for the main vibrational modes. The dominating band in the RR spectra of PEV^0 is located at 1658 cm^{-1} (mode 63) and presents the same atomic displacements in the external pyridinium rings as in MV^0. There are also four additional intense peaks above 1200 cm^{-1} - at 1565 cm^{-1} (mode 61), 1472 cm^{-1} (mode 60), 1363 cm^{-1} (mode 50), and 1234 cm^{-1} (mode 46). Like mode 63, mode 61 corresponds to CCH wagging plus CC stretching but within the central phenylene ring, so that it is specific to PEV^0. Then comes mode 60 characterized by CCH wagging and CC inter-ring stretching motions, like in MV^0. Besides the opposite phase between the CCH wagging and CC inter-ring stretching motions mode 50 (1363 cm^{-1}) is similar to mode 60 and its relative RR activity is larger for PEV^0 than MV^0. This is attributed to the larger component of CC inter-ring stretching motions. The band at 1234 cm^{-1} (mode 46) is predominantly described by CCH wagging motion. It displays a modest RR intensity in MV^0, but is one of the most important in PEV^0. Another RR signature of PEV^0 is the doublet in the region around 900-1000 cm^{-1} formed by the peaks at 947 cm^{-1} (mode 33) and 987 cm^{-1} (mode 34). Although at lower frequency, these modes also include CC inter-ring stretching and match the quinoid-aromatic distortion, which explains their coupling with the electronic excitation. These modes result from mode 34 (~994 cm^{-1}) in MV^0. The last resonantly enhanced mode is located at 743 cm^{-1} (mode 24) and displays ring breathing character.

Figure 6. Resonance Raman spectra of PEV^0 simulated at different incident light energies by using SA2-CASSCF ground and excited state geometries in combination with MP2 ground state vibrational normal modes. The energies are successively set to to E_{0e}-0.17 eV (579 nm), E_{0e}-0.09 eV (559 nm), E_{0e} (537 nm), E_{0e}+0.09 eV (517 nm), E_{0e}+0.17 eV (500 nm), E_{0e}+0.30 eV (475 nm), E_{0e}+0.39 eV (459 nm) and E_{0e}+0.47 eV (446 nm). The Raman bands are represented by Lorentzian functions with FWHM set to 10 cm^{-1}.

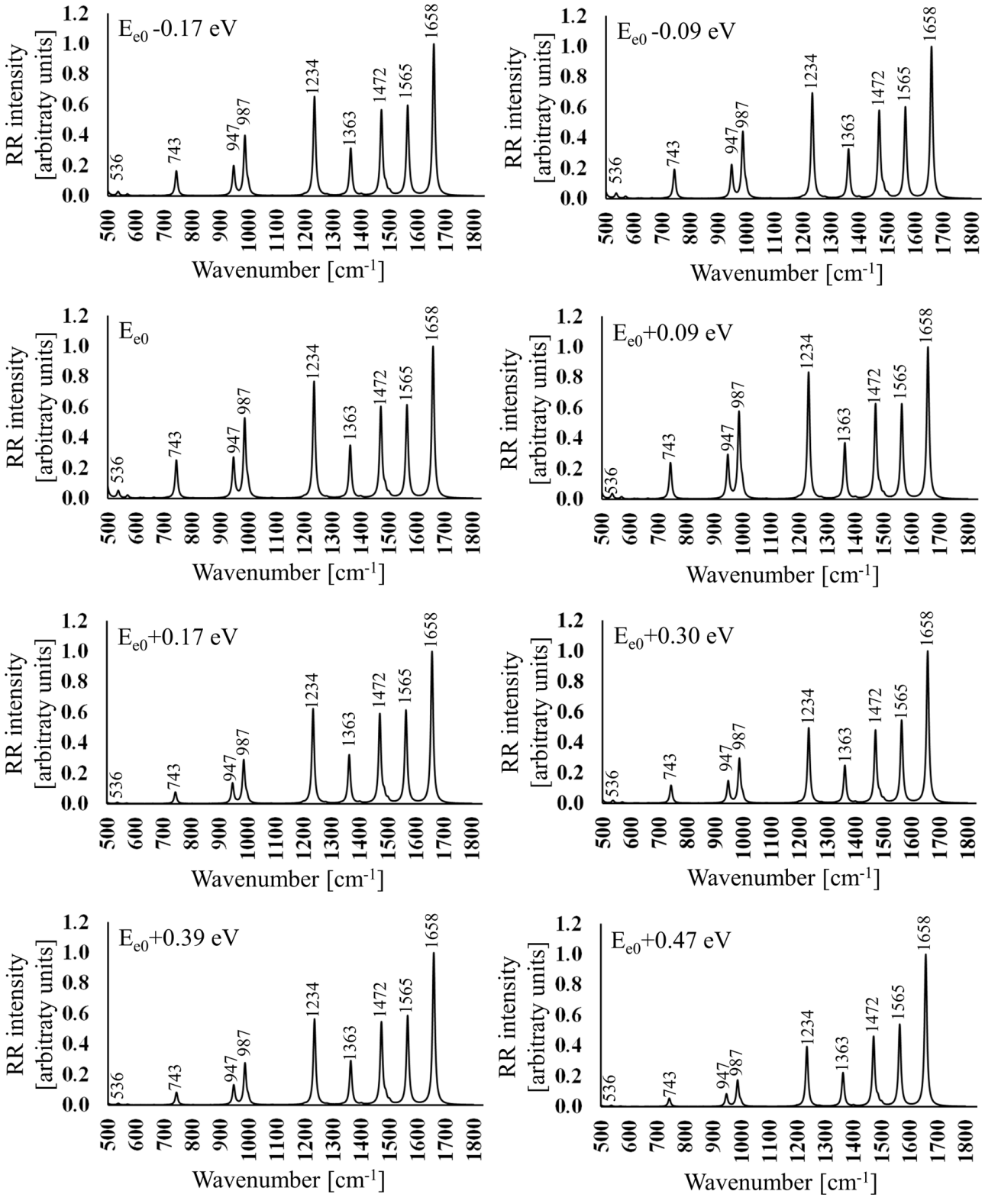

Figure 7. Resonance Raman excitation profiles for representative modes of PEV^0 simulated by using the SA2-CASSCF ground and excited state geometries in combination with MP2 ground state vibrational normal modes. Lines are guides to the eyes.

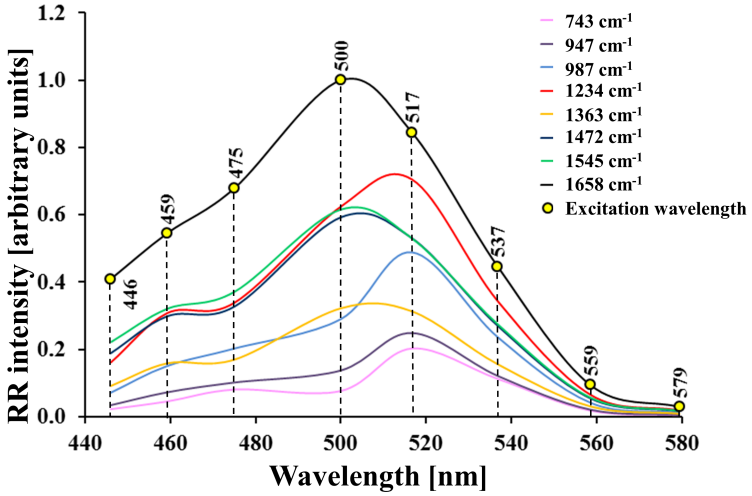

4. Further Discussions, Conclusions, and Outlook

The resonant Raman and UV/vis absorption spectra of methyl viologen and phenylene-extended viologen in their neutral state have been simulated using multiconfigurational wavefunction methods. The use of such computational approaches was dictated by the diradicaloïd character of these compounds. For methyl viologen, comparison with experimental data has been carried out, evidencing a good agreement for the UV/vis absorption vibronic structure, provided dynamic correlation is accounted for to get the vibrational frequencies and normal modes. To some extent, the agreement with experiment is also good for the RR spectrum and the differences have been attributed to the presence in the experimental spectrum of surface-enhanced effects due to adsorption on the electrodes. The simulations have then highlighted the evolution of these spectra upon inserting a phenylene group between the pyridinium units. First, in the UV/vis absorption spectrum, the relative intensity of the second band with respect to the 0-0 band increases with the extension of the viologen and additional strong bands are observed in the RR spectrum. Then, the RR excitation profiles of the phenylene-extended viologen present less structure than in the case of methyl viologen where the mode intensities can strongly depend on the incident light wavelength. These differences are signatures of the extension of the effective conjugation length as well as of the increase of diradical character and can be compared with those reported in the literature for similar compounds. So, in the case of oligo-*p*-phenylenes it has been demonstrated that the

intensity ratio between the (non-resonant) Raman bands associated with the CC inter-ring stretching and the CCH wagging modes decreases in parallel with the extension of the effective conjugation length and also decreases upon increasing the laser energy towards the resonant regime.[22] Looking at the 900-1800 cm^{-1} window, mode 46 describes CCH wagging motions and has negligible contribution from the CC intra- and inter-ring stretching motions, which are very sensitive to the conjugation length (Figure 2). It can therefore be used as reference with respect to those modes associated with different amounts of CC intra- and inter-ring stretching motions (modes N = 34, 50, 60, and 63). The I_N/I_{46} RR intensity ratios and their evolutions as a function of the excitation energy (Table 5) display large variations upon going from MV^0 to PEV^0: increasing the conjugation length leads to a decrease in the I_{63}/I_{46}, I_{60}/I_{46} and I_{34}/I_{46} ratios. In addition, these ratios depend on the excitation energies, and typically get smaller for excitation energies close to E_{e0}. Further investigations on the RR signatures of other neutral viologen or related compounds with different degrees of diradical character are, however, needed to tell how much these signatures can account for differences in the diradical character.

Table 5. RR I_N/I_{46} (N = 63, 60, 50, and 34) ratios for MV^0 and PEV^0 obtained at different excitation energies (with respect to E_{e0}) with the MP2 approach.

	-0.17 eV	**-0.09 eV**	**0.0**	**+0.09 eV**	**+0.17 eV**	**+0.30 eV**	**+0.39 eV**	**+0.47 eV**
					I_{63}/I_{46}			
MV^0	15.60	14.56	12.57	10.86	62.37	18.32	29.54	25.20
PEV^0	1.53	1.44	1.30	1.20	1.60	2.00	1.77	2.54
					I_{60}/I_{46}			
MV^0	4.08	3.87	0.91	3.11	13.53	4.40	7.17	5.48
PEV^0	0.87	0.84	0.79	0.75	0.95	0.97	0.97	1.17
					I_{50}/I_{46}			
MV^0	0.41	0.40	0.37	0.36	0.81	0.41	0.56	0.46
PEV^0	0.48	0.47	0.45	0.44	0.52	0.50	0.52	0.57
					I_{34}/I_{46}			
MV^0	2.28	2.41	2.74	2.80	0.47	2.29	1.12	1.92
PEV^0	0.61	0.64	0.69	0.69	0.46	0.60	0.49	0.44

This investigation on the vibronic effects in viologens is also related to recent studies on nonlinear optical (NLO) materials. Indeed, it has been recently demonstrated that compounds with

intermediate value of diradical character (~0.5) possess larger values of second hyperpolarizability and hence represent promising NLO materials.[23] In this respect, this paper reveals that the introduction of a phenylene bridge leads to an increase in the diradical character. The latter is defined as twice the weight of the doubly-excited configuration in the singlet ground state[24] and is estimated to be 0.32 for MV^0 and 0.42 for PEV^0 (SS-CASSCF CI vectors in Table S1), therefore, predicting that extended viologens are promising NLO compounds.

Acknowledgements

J.R. thanks the F.R.S. - FNRS for her postdoctoral fellowship under convention N° 1.5133.12. V.L. thanks the F.R.S.-FNRS for his Research Associate position. The calculations were performed on the computing facilities of the Consortium des Équipements de Calcul Intensif (CÉCI), in particular those of the Plateforme Technologique de Calcul Intensif (PTCI) installed in the University of Namur, for which we gratefully acknowledge financial support of the FNRS-FRFC (Convention No. 2.4.617.07.F and 2.5020.11).

References

1 (a) Z. G. Soos, D. S. Galvão and S. Etemad, *Adv. Mater.*, 1994, **6**, 280-287; (b) M. Klessinger and J. Michl, 'Excited states and photochemistry of organic molecules', VCH Publishers, New York, 1995; (c) J. L. Brédas, J. E. Norton, J. Cornil, and V. Coropceanu, *Acc. Chem. Res.*, 2009, **42**, 1691-1699.

2 (a) A. C. Albrecht, *J. Chem. Phys.*, 1961, **34**, 1476-1487; (b) E. J. Heller, R. L. Sundberg and D. Tannor, *J. Phys. Chem.*, 1982, **86**, 1822-1833; (c) A. B. Myers, *Chem. Rev*. (Washington, D.C.), 1996, **96**, 911-926; (d) A. M. Kelley, *J. Phys. Chem. A*, 1999, **103**, 6891-6903; (d) A. M. Kelley, *J. Phys. Chem. A*, 2008, **112**, 11975-11991.

3 (a) J. Neugebauer, E. J. Baerends, E. V. Efremov, F. Ariese and C. Gooijer, *J. Phys. Chem. A*, 2005, **109**, 2100-2106; (b) C. Herrmann, J. Neugebauer, M. Presselt, U. Uhlemann, M. Schmitt, S. Rau, J. Popp, and M. Reiher, *J. Phys. Chem. B*, 2007, **111**, 6078-6087; (c) J. Guthmuller and B. Champagne, *J. Chem. Phys.*, 2007, **127**, 164507 (1-11); A. A. Jarzecki, *J. Phys. Chem. A*, 2009, **113**, 2926-2934; (d) V. Barone, J. Bloino, M. Biczysko, and F. Santoro, *J. Chem. Theory Comput.*, 2009, **5**, 540-554; (e) J. Guthmuller, B. Champagne, C. Moucheron and A. Kirsch-De Mesmaeker, *J. Phys. Chem. B*, 2010, **114**, 511-520; (f) R. Scholtz, L. Gisslen, B. E. Schuster, M. B. Casu, T. Chassé, U. Heinemeyer and F. Schreiber, *J. Chem. Phys.*, 2011, **134**, 014504 (1-11); (g) W. Wu, Z. Cao and Y. Zhao, *J. Chem. Phys.*, 2012, **136**, 114305 (1-9); (h) T. Petrenko and F. Neese, *J. Chem. Phys.*, 2012**,** **137**, 234107 (1-19); (i) D. W. Silverstein, N. Govind, H. J. J. van Dama and L. Jensen, *J. Chem. Theory Comput.*, 2013, **9**, 5490-5503.

4 (a) C. Lapouge, G. Buntinx and O. Poizat, *J. Phys. Chem. A*, 2002, **106**, 4168-4175; (b) P. Altoe, F. Bernardi, M. Garavelli, G. Orlandi and P. Negri, *J. Am. Chem. Soc.*, 2005, **127**, 3952-3963; (c) T. Petrenko and F. Neese, *J. Chem. Phys.*, 2007, **127**, 164319 (1-15); (d) J. Guthmuller, *J. Chem. Theory Comput.*, 2011, **7**, 1082-1089; (f) S. Kupfer, J. Guthmuller and L. Gonzalez, *J. Chem. Theor. Comput.*, 2013, **9**, 543-554.

5 (a) A. Konishi, Y. Hirao, M. Nakano, A. Shimizu, E. Botek, B. Champagne, D. Shiomi, K. Sato, T. Takui, K. Matsumoto, H. Kurata and T. Kubo, *J. Am. Chem. Soc.*, 2010, **132**, 11021-11023; (b) M. B. Smith and J. Michl, *Chem. Rev.*, 2010, **110**, 6891-6936; (c) C. Lambert, *Angew. Chem. Int. Ed.*, 2011, **50**, 1756-1758; (d) Z. Zeng, Y. M. Sung, N. Bao, D. Tan, R. Lee, J. L. Zafra, B. S. Lee, M. Ishida, J. Ding, J. T. L. Navarrete, Y. Li, W. Zeng, D. Kim, K. W. Huang, R. D. Webster, J. Casado and J. Wu, *J. Am. Chem. Soc.*, 2012, **134**, 14513-14525; (e) Z. Sun and J. Wu, *J. Mater. Chem.*, 2012, **22**, 4151-4160; (f) A. Konishi, Y. Hirao, K. Matsumoto, H. Kurata, R. Kishi, Y. Shigeta, M. Nakano, K. Tokunaga, K. Kamada and T. Kubo, *J. Am. Chem. Soc.*, 2013, **135**, 1430-1437.

6 (a) S. R. Gonzalez, B. Nieto-Ortega, C. Gonzalez, V. Lloveras, J. J. Novoa, F. Mota, J. Vidal-Gancedo, C. Rovira, J. del C. Veciana, M. Taravillo, V. G. Baonza, N. Lopez and J. Casado, *J. Chem. Phys.*, 2014, **140**, 164903 (1-9); (b) J. Casado, R. P. Ortiz and J. T. L. Navarrete, *Chem. Soc. Rev.*, 2012, **41**, 5672-5686; (c) S. Di Motta, F. Negri, D. Fazzi, C. Castiglioni and E. V. Canesi, *J. Phys. Chem. Lett.*, 2010, **1**, 3334-3339; (d) D. Fazzi, E. V. Canesi, F. Negri, C. Bertarelli and C. Castiglioni, *ChemPhysChem*, 2010, **11**, 3686-3695.

7 (a) P. M. S. Monk, *The Viologens: Physicochemical Properties, Synthesis and Applications of the Salts of 4,4'-Bipyridine*, Wiley, Chichester, 1998; (b) K. Takahashi, T. Nihira, K. Akiyama, Y. Ikegami and E. Fukuyo, *J. Chem. Soc. Comm.*, 1992, 620-622; (c) A. Funston, J. P. Kirby, J. R. Miller, L. Pospíšil, J. Fiedler, M. Hromadová, M. Gál, J. Pecka, M. Valášek, Z. Zawada, P. Rempala and J. Michl, *J. Phys. Chem. A*, 2005, **109**, 10862-10869; (d) M. Valášek, J. Pecka, J. Jindřich, G. Calleja, P. R. Craig and J. Michl, *J. Org. Chem.*, 2005, **70**, 405-412; (f) L. Pospíšil, J. Fiedler, M. Hromadová, M. Gál, M. Valášek, J. Pecka and J. Michl, *J. Electrochem. Soc*., 2006, **153**, E179.

8 (a) H. L. Anderson, *Nature Chemistry*, 2010, **2**, 12-13; (b) F. Scholz, L. Dworak, V. V. Matylitsky and J. Wachtveitl, *ChemPhysChem*, 2011, **12**, 2255-2259; (c) V. Kolivoška, M. Gál, L. Pospíšil, M. Valášek and M. Hromadová, *Phys. Chem. Chem. Phys.*, 2011, **13**, 11422-11429; (d) L. Dworak, V. V. Matylitsky, V. V. Breus, M. Braun; T. Basché and J. Wachtveitl, *J. Phys. Chem. C*, 2011, **115**, 3949-3955; (e) V. Kolivoška, M. Valášek, M. Gál, R. Sokolová, J. Bulíčková, L. Pospíšil, G. Mészáros and M. Hromadová, *J. Phys. Chem. Lett.*, 2013, **4**, 589-595; (f) A. C. Fahrenbach, S. C. Warren, J. T. Incorvati, A. J. Avestro, J. C. Barnes, J. F. Stoddart and B. A. Grzybowski, *Adv. Mater.*, 2013, **25**, 331-348; (g) W. T. Tsai, *Toxicol. Environ. Chem.*, 2013, **95**, 197-206; (h) P. -Y. Chen, C. -S. Chen and T. -H. Yeh, *J. Appl. Polym. Sci.*, 2014, 40485 (1-6).

9 (a) M. P. Makowski and W. L. Matticet, *Polymer*, 1993, **34**, 1606-1612; (b) C. Majumder, H. Mizuseki and Y. Kawazoe, *Mater. Trans.*, 2001, **42**, 2276-2278; (c) P. Stipa, *Spectrochim. Acta Part A*, 2006, **64**, 653-659; (d) A. D. Matteo, *Chem. Phys. Lett.*, 2007, **439**, 190-198; (e) W. Haiss, T. Albrecht, H. van Zalinge, S. J. Higgins, D. Bethell, H. Höbenreich, D. J. Schiffrin, R. J. Nichols, A. M. Kuznetsov, J. Zhang, Q. Chi and J. Ulstrup, *J. Phys. Chem. B*,

2007, **111**, 6703-6712; (f) J. Casado, S. Patchkovskii, M. Z. Zgierski,; L. Hermosilla, C. Sieiro, M. Moreno Oliva and J. T. L. Navarrete, *Angew. Chem. Int. Ed.*, 2008, **47**, 1443-1446; (g) G. Saielli, *J. Phys. Chem. A*, 2008, **112**, 7987-7995; (h) S. F. Haddad, B. F. Ali, R. H. Al-Far, J. N. Dawoud and M. I. Alomari, *Polyhedron*, 2010, **29**, 1109-1115; (i) N. Lebedev, S. Trammell, W. Dressick, G. S. Kedziora, I. Griva and J. M. Schnur, *Photochem. Photobiol.*, 2011, **87**, 1024-1030; (j) M. E. Alberto, B. C. De Simone, S. Cospito, D. Imbardelli, L. Veltri, G. Chidichimo and N. Russo, *Chem. Phys. Lett.* 2012, **552**, 141-145.

10 J. Romanova, V. Liégeois, B. Champagne, *J. Phys. Chem. C*, 2014, **118**, 12469-12484.

11 T. M. Bockman and J. K. Kochi, *J. Org. Chem.*, 1990, **55**, 4127-4135.

12 Q. Feng and T. M. Cotton, *J. Phys. Chem.*, 1986, **90**, 983-987.

13 S. Ghoshal, T. Lu, Q. Feng, T. M. Cotton, *Spectrochim. Acta*, *Part A*, 1988, **44**, 651-660.

14 Q. Feng, W. Yue and T. M. Cotton, *J. Phys. Chem.*, 1990, **94**, 2082-2089.

15 H. -J. Werner, P. J. Knowles, G. Knizia, F. R. Manby, M. Schütz, P. Celani, T. Korona, R. Lindh, A. Mitrushenkov, G. Rauhut, K. R. Shamasundar, T. B. Adler, R. D. Amos, A. Bernhardsson, A. Berning, D. L. Cooper, M. J. O. Deegan, A. J. Dobbyn, F. Eckert, E. Goll, C. Hampel, A. Hesselmann, G. Hetzer, T. Hrenar, G. Jansen, C. Köppl, Y. Liu, A. W. Lloyd, R. A. Mata, A. J. May, S. J. McNicholas, W. Meyer, M. E. Mura, A. Nicklass, D. P. O'Neill, P. Palmieri, D. Peng, K. Pflüger, R. Pitzer, M. Reiher, T. Shiozaki, H. Stoll, A. J. Stone, R. Tarroni, T. Thorsteinsson, and M. Wang, *MOLPRO, version 2012.1, a package of ab initio programs*, 2012.

16 (a) H. J. Werner and P.J. Knowles, *J. Chem. Phys.*, 1985, **82**, 5053-5063; (b) P. J. Knowles and H. J. Werner, *Chem. Phys. Lett.*, 1985, **115**, 259-265; (c) P. Celani and H.J. Werner, J. *Chem. Phys.*, 2000, **112**, 5546-5557.

17 M. J. Frisch, G. W. Trucks, H. B. Schlegel, G. E. Scuseria, M. A. Robb, J. R. Cheeseman, G. Scalmani, V. Barone, B. Mennucci, G. A. Petersson, H. Nakatsuji, M. Caricato, X. Li, H. P. Hratchian, A. F. Izmaylov, J. Bloino, G. Zheng, J. L. Sonnenberg, M. Hada, M. Ehara, K. Toyota, R. Fukuda, J. Hasegawa, M. Ishida, T. Nakajima, Y. Honda, O. Kitao, H. Nakai, T. Vreven, J. A. Montgomery, Jr., J. E. Peralta, F. Ogliaro, M. Bearpark, J. J. Heyd, E. Brothers, K. N. Kudin, V. N. Staroverov, R. Kobayashi, J. Normand, K. Raghavachari, A. Rendell, J. C. Burant, S. S. Iyengar, J. Tomasi, M. Cossi, N. Rega, J. M. Millam, M. Klene, J. E. Knox, J. B. Cross, V. Bakken, C. Adamo, J. Jaramillo, R. Gomperts, R. E. Stratmann, O. Yazyev, A. J. Austin, R. Cammi, C. Pomelli, J. W. Ochterski, R. L. Martin, K. Morokuma, V. G. Zakrzewski, G. A. Voth, P. Salvador, J. J. Dannenberg, S. Dapprich, A. D. Daniels, Ö. Farkas, J. B. Foresman, J. V. Ortiz, J. Cioslowski, and D. J. Fox, *Gaussian 09, Revision A.01*, Gaussian, Inc., Wallingford CT, 2009.

18 W. L. Peticolas and T. Rush III, *J. Comput. Chem.*, 1995, **16**, 1261-1270.

19 P. T. Ruhoff, *Chem. Phys.*, 1994, **186**, 355-374.

20 M. Forstert, R. B. Girling and R. E. Hester, *J. Raman Spectrosc.*, 1982, **12**, 36-48.

21 T. Lu and T. M. Cotton, *J. Phys. Chem.*, 1987, **91**, 5978-5985.

22 G. Heimel, D. Somitsch, P. Knoll, J.- L. Brédas and E. Zojer, *J. Chem. Phys.*, 2005, **122**, 114511 (1-9).

23 (a) M. Nakano, R. Kishi, T. Nitta, T. Kubo, K. Nakasuji, K. Kamada, K. Ohta, B. Champagne, E. Botek and K. Yamaguchi, *J. Phys. Chem. A*, 2005, **109**, 885-891; (b) K. Kamada, K. Ohta, A. Shimizu, T. Kubo, R. Kishi, H. Takahashi, E. Botek, B. Champagne and M. Nakano, *J. Phys. Chem. Lett.*, 2010, **1**, 937-940.

24 M. Head-Gordon, *Chem. Phys. Lett.*, 2003, **372**, 508-511.